Reliability Engineering and System Safety 244 (2024) 109954

Contents lists available at ScienceDirect

Reliability Engineering and System Safety

journal homepage: www.elsevier.com/locate/ress

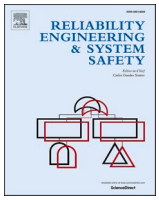

A robust health prediction using Bayesian approach guided by physical constraints

Hyung Jun Park [a], Nam H. Kim [b], Joo-Ho Choi [c,*]

[a] Department of Aerospace and Mechanical Engineering, Korea Aerospace University, Gyeong gi-do, 10540, Korea
[b] Department of Mechanical and Aerospace Engineering, University of Florida, Gainesville, USA
[c] School of Aerospace and Mechanical Engineering, Korea Aerospace University, Gyeong gi-do, 10540, Korea

ARTICLE INFO

Keywords:
Prognostics
Bayesian inference
Remaining useful life
Low-fidelity physics information
Uncertainty quantification

ABSTRACT

Accurately predicting the remaining useful life (RUL) of industrial machinery is crucial for ensuring their reliability and safety. Prognostic methods that rely on Bayesian inference, such as the Bayesian method (BM), Kalman and Particle filter (KF, PF), have been extensively studied for RUL predictions. However, these algorithms can be affected by noise when training data are limited or uncertainty when empirical models are employed in place of accurate physics models. As a result, this can lead to significant prediction errors or even infeasible RUL predictions. To overcome this challenge, three different approaches are proposed to guide the Bayesian framework by incorporating low-fidelity physical information. The key idea is to impose inequality constraints to reduce sensitivity to noisy observations and achieve robust prediction. To evaluate the feasibility of the approaches, their performance is evaluated by a numerical example and real case study for drone motor degradation.

1. Introduction

The improvement of manufacturing productivity in smart factory depends on Prognostics and health management (PHM) techniques, which enable prediction of the machinery remaining useful life (RUL) to prevent unexpected failure and ensure smooth operation. To perform accurate RUL prediction, not only health indicator (HI) needs to be extracted from the sensor signals, but also require robust prognostic algorithms to estimate or train the degradation model using up to date HIs and predict future degradation trajectory [1].

For prognostics, two types of approaches are commonly used: data-driven and model-based approaches [2,3]. Data-driven approaches use historical datasets to identify degradation patterns and predict the future degradation behavior of machinery using artificial intelligence (AI) methods such as neural network (NN) [4] and fuzzy logic [5] or statistical methods including the Gaussian process (GP) regression [6], long short-term memory (LSTM) network [7] and support vector machine (SVM) [8]. Although data-driven approaches are free from the in-depth knowledge of degradation physics, they require a huge amount of training data, and insufficient training data may lead to poor accuracy and large training uncertainty to make proper decision-making. In contrast, model-based approaches use a physical model that describes machinery degradation behavior and enables more accurate and long-term prediction. For instance, a physical model such as Paris-Erdogan or Huang's model is utilized to predict the degradation process of bearings [9] and crack growth [10]. Bayesian filtering algorithms such as the Bayesian method (BM) [11], Kalman filter (KF) [12] and Particle filter (PF) [13] are widely used to estimate these model parameters. However, complex machinery systems with various components and failure mechanisms present challenges for developing high-fidelity physical models. Recently, a comprehensive review has been undertaken to assess advanced prognostics method and direction for prognostic approach, highlighting gaps in their design, development, and decision-making perspectives [14,15].

Though both data-driven and model-based approaches have shown good RUL prediction performances in various fields, their limitations

Abbreviations: BM, Bayesian method; CDF, cumulative density function; C.I., confidence interval; HI, health indicator; KF, Kalman filter; MAE, mean absolute error; MCMC, Markov-chain Monte Carlo; PF, particle filter; PI, prediction interval; PICP, predict interval coverage probability; PINAW, prediction interval normalized average width; PMD, parrot mambo drone; PDF, probability density function; RPF, regularized particle filter; RUL, remaining useful life; UAV, unmanned aerial vehicle.

* Corresponding author.
E-mail address: jhchoi@kau.ac.kr (J.-H. Choi).

https://doi.org/10.1016/j.ress.2024.109954
Received 18 June 2023; Received in revised form 13 January 2024; Accepted 15 January 2024
Available online 17 January 2024

have impeded the implementation in practical applications. Thus, hybrid approaches have been developed in both approaches. The data-driven approaches incorporated physical laws into data-driven methods by integrating essential mathematical information into a machine learning framework [16–18]. However, a high-fidelity physical model is still required to be embedded into the machine learning framework [19,20]. In model-based approaches, simple but empirical mathematical models such as the single exponential model [21,22], polynomial model [23], dual-exponential model [24,25] or transformation of multiple models [26] can be used as an alternative. These models do not possess specific physical meaning but can capture the degradation process over time and can be selected based on a run-to-failure history [27]. For instance, exponential models are often used to represent the gradual wear and tear of components, while polynomial models may capture more complex patterns of degradation [28]. Moreover, the Bayesian inference algorithms like BM and PF not only accurately estimate model parameters but also characterize prediction uncertainties. However, empirical models with conventional Bayesian inference algorithms require substantial data to robustly estimate the degradation physics and may lead to unrealistic RUL prediction in the presence of non-monotonic data influenced by measurement noise. Based on the existing survey, this paper proposes a method to enforce physical constraints in Bayesian approach to capture complex degradation evolution and enhance noise insensitivity even in early degradation stage with limited data. To the best of our knowledge, these issues have not been extensively discussed in the prognostics using Bayesian inference algorithms.

A few studies have addressed incorporating constraints in the Bayesian algorithms to improve RUL prediction. For instance, Son et al. [29] applied constraints in KF to generate a truncated probability density function (PDF) and minimize the impact of large measurement noise on RUL prediction. They established constraint ranges for model parameters to achieve truncated posterior PDF and applied to automotive lead-acid battery failure predictions. Tang et al. [30] addressed the gradient-correction method in the calculation of weights in the PF algorithm. The gradient corrector is regulated by an effective base model obtained from historical datasets. However, acquiring predefined parameter ranges through expert knowledge remains challenging and may restrict adaptation to degradation trends differing from those observed in historical datasets. Recently, Downey et al. [31] proposed non-linear least square method with dynamic bounds for parameters, enabling the tracking of multiple aging mechanisms and demonstrated online RUL prediction using eight batteries. Nevertheless, the fluctuation of monitoring data during degradation introduces challenges to parameter estimation, leading to significant prediction errors. Addressing this issue, Yu et al. [32] utilized B-spline model updated through constrained PF, eliminating particles that do not meet the monotonic constraints after resampling. However, truncating the PDF after obtaining the unconstrained posterior distribution may reduce the number of samples to estimate posterior distribution. Moreover, existing studies have primarily focused on constraints within the interpolation region, neglecting the extrapolation region for prediction. Li et al. [33] introduced a self-constraint state-space estimator to acquire a constraint curve in the future time but required trend of the historical datasets to set constraints.

To address the above issues, this research proposes three distinct methods to incorporate physical constraints into the traditional Bayesian prognostic framework aiming to reduce sensitivity to local noisy measurements and improve RUL prediction performance. The first method involves giving physical constraints based on initial prior knowledge of degradation model parameters. However, unlike other studies, this knowledge is identified by the monotonicity and curvature of the model. The second method involves constraining the acceptance criteria in a sampling method to generate samples for posterior distribution without reducing its number. The third method similarly constrains a sampling method by giving penalties to the cost function (i.e. likelihood) to act as a regularization term. These methods are applied to two different prognostic algorithms: the BM and PF. In addition, physical constraints are applied to extrapolation region that training data cannot cover during the parameter estimation. Finally, the prediction performance is robustly compared addressing the data uncertainty due to noise randomness. The main contributions of our work are summarized as follows:

- Three different methods to integrate physical constraints into Bayesian inference-based prognostic algorithms is proposed.
- Physical constraints in the extrapolation region are also considered in optimizing the degradation parameter estimation in the Bayesian framework.
- The data uncertainty is quantified using synthetic measurement data, providing a robust evaluation of the proposed method.
- Numerical and a real case study are presented to demonstrate the performance of the proposed method, particularly when dealing with noisy measurement data and early-stage predictions.

The article is organized as follows. In Section 2, prognostic algorithms based on the Bayesian framework and the definition of physical constraints for prognosis are briefly introduced. Then, in Section 3, three different approaches to embedding physical constraints are proposed in detail with the implementation procedure for each prognostic algorithm. In Section 4, the metrics to evaluate the prediction accuracy and uncertainty with the data uncertainty are addressed. In Sections 5 and 6, the proposed methods are applied to numerical simulation and a real case study for drone motor degradation, respectively, followed by Conclusions in Section 7.

2. Model-based prognostics

This section introduces a brief overview of the various parameter estimation algorithms used in model-based prognostics. These algorithms involve the following three steps: (1) identifying or developing a physical model that describes the degradation dynamics, (2) estimating model parameters by fitting data acquired at a sequence of times/cycles, and (3) extrapolating the model to predict the trend and RUL at future times/cycles [34]. The BM is an overall Bayesian approach, while the PF is a recursive Bayesian approach to estimating the model parameters. Further details are discussed in the following sections.

2.1. BM-based approach

In BM, the joint posterior PDF of model parameters at the current cycle is obtained by a single equation, in which all the likelihoods of measurements are multiplied. In detail, let $\boldsymbol{\theta}$ be the vector of unknown model parameters including measurement noise σ, and $\boldsymbol{y}_{1:k}$ is the vector of observed data up to current cycle k. The joint posterior PDF is obtained by multiplying the prior PDF and the likelihood as

$$p(\boldsymbol{\theta}|\boldsymbol{y}_{1:k}) \propto p(y_1|\boldsymbol{\theta}) \times p(y_2|\boldsymbol{\theta}) \cdots p(y_k|\boldsymbol{\theta}) \times p(\boldsymbol{\theta}) = p(\boldsymbol{y}_{1:k}|\boldsymbol{\theta}) p(\boldsymbol{\theta}) \tag{1}$$

$$p(\boldsymbol{y}_{1:k}|\boldsymbol{\theta}) = \left(\sigma^2\right)^{-k/2} \exp\left\{ -\frac{1}{2\sigma^2} (\boldsymbol{y}_{1:k} - \widehat{\boldsymbol{y}}_{1:k})^T (\boldsymbol{y}_{1:k} - \widehat{\boldsymbol{y}}_{1:k}) \right\} \tag{2}$$

where $p(\boldsymbol{\theta})$ is the prior PDF of parameters, $p(\boldsymbol{y}_{1:k}|\boldsymbol{\theta})$ is the multiplied likelihood of observed data conditional on the given parameter value $\boldsymbol{\theta}$, and $\widehat{\boldsymbol{y}}_{1:k}$ is the vector of model predictions.

Once the expression of the posterior PDF is obtained from Eq. (1), a sampling method using the Markov-chain Monte Carlo (MCMC) is employed to draw N samples of the parameters. Fig. 1 summarizes the BM process with sampling using the Metropolis-Hasting (M-H) algorithm, which is a typical method of MCMC. First, the user sets the initial value for parameters $\boldsymbol{\theta}_0$, the initial prior distribution $p(\boldsymbol{\theta})$, and the weight $\boldsymbol{w}$ which is a vector of values for the sampling interval of the

BM process

- **Initial settings**

: Set initial value $\boldsymbol{\theta_0}$, initial prior distribution $p(\boldsymbol{\theta})$, weight $\boldsymbol{w}$

- **MH algorithm**

: For $i = 1, \ldots, N$

- Generate a new sample from the proposal distribution

$$\boldsymbol{\theta}^* \sim g(\boldsymbol{\theta}^* | \boldsymbol{\theta}^{i-1}) = U(\boldsymbol{\theta}^{i-1} - \boldsymbol{w}, \boldsymbol{\theta}^{i-1} + \boldsymbol{w})$$

- Generate acceptance sample $u \sim U(0,1)$

- If $u < Q(\boldsymbol{\theta}^{i-1}, \boldsymbol{\theta}^*)$

$\boldsymbol{\theta}^i = \boldsymbol{\theta}^*$

Else

$\boldsymbol{\theta}^i = \boldsymbol{\theta}^{i-1}$

Fig. 1. Illustration of BM process with MCMC.

proposal distribution $g(\boldsymbol{\theta}^* | \boldsymbol{\theta}^{i-1})$. Then a new sample $\boldsymbol{\theta}^*$ is drawn from the proposal distribution and the selected based on the following acceptance criterion:

$$Q(\boldsymbol{\theta}^{i-1}, \boldsymbol{\theta}^*) = \mathbf{min}\left\{1, \frac{p(\boldsymbol{\theta}^*|\boldsymbol{y}) g(\boldsymbol{\theta}^{i-1}|\boldsymbol{\theta}^*)}{p(\boldsymbol{\theta}^{i-1}|\boldsymbol{y}) g(\boldsymbol{\theta}^*|\boldsymbol{\theta}^{i-1})}\right\} = \mathbf{min}\left\{1, \frac{p(\boldsymbol{\theta}^*|\boldsymbol{y})}{p(\boldsymbol{\theta}^{i-1}|\boldsymbol{y})}\right\} \quad (3)$$

where the proposal distribution can be removed since it is a symmetric distribution. More detailed explanations are given in references [35,36].

2.2. PF-based approach

The PF also follows Bayes' theorem where the posterior distribution of model parameters is approximated with many particles (or samples) and their weights. Unlike the BM, the PF is based on the filtering technique that updates parameters recursively by taking one measurement at a time.

The general PF requires a state transition model f and measurement model h as

$$x_k = f(x_{k-1}, \boldsymbol{\beta}_k) + \omega_k \quad (4)$$

$$y_k = h(x_k) + v_k \quad (5)$$

where k is the cycle index, x_k is the degradation state, $\boldsymbol{\beta}_k$ is a vector of degradation model parameters and y_k is measurement. ω_k and v_k are process and measurement noise, respectively. The process noise v_k is ignored as it can be handled through the uncertainty in model parameters and the measurement noise ω_k is assumed Gaussian, i.e., $\omega_k \sim N(0, \sigma_k)$, where σ_k is the unknown standard deviation. Thus, the unknown parameters become $\boldsymbol{\theta} = [x, \boldsymbol{\beta}, \sigma]$, including the state which is obtained based on the model parameters and measurement noise.

The process of PF begins with drawing random samples for the unknown parameters with the number of particles N from the assumed initial PDF. Then the three steps are followed as shown in Fig. 2: Prediction—the prior PDF $p(\boldsymbol{\theta}_k)$ at the current cycle k is obtained from the posterior distribution of the previous cycle $k-1$. The degradation state is predicted with the model f while the model parameters and standard deviation are unchanged; Update—the likelihood from the measured data y_k at the current step is calculated as

$$w_k^i \propto p(y_k | x_k^i, \boldsymbol{\beta}_k^i, \sigma_k^i) \propto p(y_k | \boldsymbol{\theta}_k^i) = \frac{1}{\sigma_k^i \sqrt{2\pi}} \exp\left[\frac{1}{2\sigma_k^{i\,2}}\left(y_k - x_k^i(\boldsymbol{\beta}_k^i)\right)^2\right] \quad (6)$$

RPF process

- **State prediction**

: For $i = 1, \ldots, N$

- Draw particles of θ_k^i using the state transition model

- **Update - weight calculation**

: For $i = 1, \ldots, N$

- Calculate the weight of the samples

$w_k^i \propto p(y_k | \boldsymbol{\theta}_k^i)$

- **Resampling – inverse CDF**

- Generate particles that approximate the posterior PDF

$p(\boldsymbol{\theta_k} | y_{1:k}) \approx \sum_{i=1}^N w_k^i K_h(\boldsymbol{\theta_k} - \boldsymbol{\theta_k^i})$,

K_h is a rescaled kernel from the symmetric kernel density functio n

Fig. 2. Illustration of RPF process.

where w_k^i is the likelihood or weight of the ith particle proportional to the PDF in Eq. (6); Resampling—the particles in the updated distribution are resampled based on their weights by duplicating or eliminating samples using the inverse cumulative distribution function (CDF) method. The resampling result corresponds to the posterior distribution at the current step and is used as a prior for the next cycle $k+1$. However, since the PF suffers from the problem of particle impoverishment, a regularized PF (RPF) is employed in this study, which uses a kernel function in the resampling step to approximate the weighted particles in continuous distribution. Further details are addressed in [13, 37].

2.3. Physical constraints

In this paper, the physical constraints based on low-fidelity physical information is used. The low-fidelity physical information is the lowest level of available physical information that represents the crude behavior of parameters for degradation [19]. For the reader's understanding, it is explained with a polynomial degradation model that will be discussed in the numerical study. The degradation model x_k is defined as:

$$x_k = C + \beta_1 t_k^2 + \beta_2 t_k^3 \text{and } y_k = x_k + \epsilon \text{ with } \epsilon \sim N(0, \sigma) \quad (7)$$

where $\boldsymbol{\beta} = [\beta_1, \beta_2]$ is model parameters, C is an initial value, t_k is cycle and y_k is measurement added by random noise ϵ following Gaussian distribution with standard deviation σ.

It is well known that in degradation, the damage state x_k should monotonically increase over the cycle (i.e. $dx/dt \geq 0$) and the slope of degradation should be a positive trend (i.e. a non-linearly increasing trend, $dx^2/dt^2 \geq 0$). These two pieces of information represent monotonicity and curvature, respectively. Thus, the physical knowledge of the constraints can be defined as

$$\begin{cases} \textit{Monotonicity}: \ \widehat{\boldsymbol{y}}_{\boldsymbol{m}} = 2\boldsymbol{\beta}_1^* \boldsymbol{t}_{T_p} + 3\boldsymbol{\beta}_2^* \boldsymbol{t}_{T_p}^2 \geq 0 \\ \textit{Curvature}: \ \widehat{\boldsymbol{y}}_{\boldsymbol{c}} = 2\boldsymbol{\beta}_1^* + 6\boldsymbol{\beta}_2^* \boldsymbol{t}_{T_p} \geq 0 \end{cases} \text{where } \boldsymbol{t}_{T_p} = [1, 2, \ldots, T_p] \quad (8)$$

where the prediction points T_p including both the interpolation (measurements) and the extrapolation regions as shown in Fig. 3. In the figure, prediction is carried out using measurements until 8 cycles which red solid line represents the medians of prediction by BM.

3. Proposed methodology

This section presents methodologies to incorporate constraints into

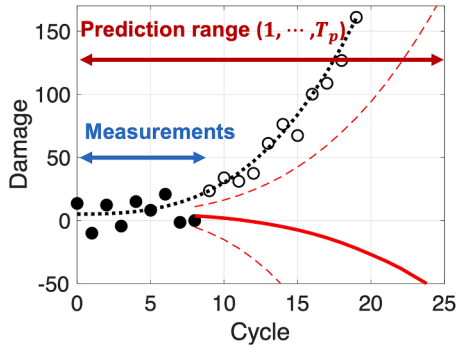

Fig. 3. Physical constraint calculation with prediction points.

the BM and PF algorithms. Fig. 4 illustrates our proposed methodology, which involves three different encoding methods to guide the prognostic algorithms using monotonicity and curvature constraints. Then prognostics performance with data uncertainty is evaluated with quantitative metrics.

3.1. Method 1: constraining the initial prior distribution

First, a simple and direct approach to incorporate physical constraints in the Bayesian approach is to apply them to the initial prior distribution. In Method 1, the initial prior distribution is established such that the constraints are satisfied in all prediction range. Unlike the most related studies that provide a prior constraint range based on expert domain knowledge, this paper identifies the range by combining the monotonicity and curvature of the damage model.

In more detail, from the polynomial damage model in Eq. (7), we intend to impose inequality constraints on the model parameters $\beta_j,\ j = 1,\ 2$ to meet the physical constraints at all prediction cycles and obtain the corresponding constraint set $\mathbb{C}$.

$$\mathbb{C} = \left\{a_j \le \beta_j \le b_j\right\}\ j = 1,\ 2 \tag{9}$$

Then the constrained prior distribution $p_c(\boldsymbol{\theta})$ is defined such that it is a uniform distribution for the BM, or initial random samples generated only in the range of $\mathbb{C}$ for the PF.

In the BM, the samples are drawn from the posterior PDF $p_c(\boldsymbol{\theta}|\boldsymbol{y}_{1:k})$ by applying constrained prior $p_c(\boldsymbol{\theta})$. The acceptance criterion for the samples is then determined based on the following constraints.

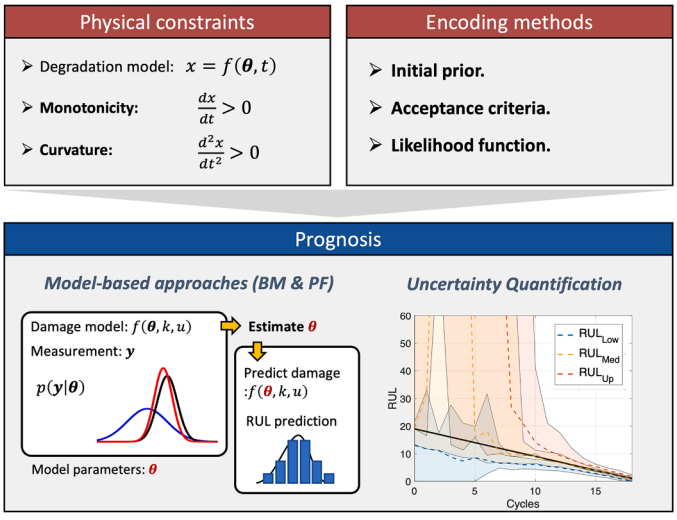

Fig. 4. The proposed methodology for prognostics guided by physical constraints.

$$Q_c\left(\boldsymbol{\theta}^{i-1}, \boldsymbol{\theta}^*\right) = \min\left\{1,\ \frac{p_c(\boldsymbol{\theta}^*|\boldsymbol{y})}{p_c\left(\boldsymbol{\theta}^{i-1}|\boldsymbol{y}\right)}\right\} \text{ where } p_c(\boldsymbol{\theta}|\boldsymbol{y}) \propto p(\boldsymbol{y}|\boldsymbol{\theta}) p_c(\boldsymbol{\theta}) \tag{10}$$

In the RPF, the samples at the initial step are drawn from the $p_c(\boldsymbol{\theta})$, and the three steps: prediction, update and resampling are followed recursively. However, since the RPF employs kernel function in the resampling step to accommodate continuous distribution, some samples may violate the constraint range. To prevent this, the truncated likelihood is considered. Fig. 5 illustrates this with an example, which shows the resampling step by inverse CDF method by (a) conventional likelihood versus (b) truncated likelihood when the parameter is constrained within the blue range. Thus, compared to Eq. (6), the truncated likelihood is defined as follows:

$$p_c\left(y_k|\boldsymbol{\theta}_k^i,\quad \boldsymbol{\theta}_k^i \in \mathbb{C}\right) = \begin{cases} p\left(y_k|\boldsymbol{\theta}_k^i\right), & \text{if } \boldsymbol{\theta}_k^i \in C \\ 0, & else \end{cases}, \tag{11}$$

3.2. Method 2: constraining the acceptance criterion

In Method 2, an additional criterion is imposed on the sampling acceptance criterion to incorporate the physical constraints. Unlike Method 1, the initial prior distribution of model parameters is not constrained, and initial samples are drawn as usual. At each cycle, a new sample drawn from the proposal distribution of BM or particles at the prediction step of PF is used to calculate $\hat{\boldsymbol{y}}_m$ and $\hat{\boldsymbol{y}}_c$. Then, the sample/particle is only accepted if it meets the following constraints.

$$\mathbb{C} = \left\{\hat{\boldsymbol{y}}_m \ge 0\ \&\ \hat{\boldsymbol{y}}_c \ge 0\right\} \tag{12}$$

In the BM, this condition is added to the acceptance criterion for $Q(\boldsymbol{\theta}^{i-1}, \boldsymbol{\theta}^*)$. In the RPF, the two constraints are calculated with the predicted particles. Then the values are used to set the boundaries $\mathbb{C}$, and the same procedure with Method 1 is used to truncate the likelihood function.

3.3. Method 3: penalizing the likelihood function

Method 3 is to incorporate the physical constraints by imposing penalties on the likelihood function when the two physical constraints, monotonicity, and curvature, are violated. As a result, the likelihoods in the BM and RPF as defined in Eqs. (2) and (6) are changed to

$$p_{c,\ BM}\left(\boldsymbol{y}_{1:k}|\boldsymbol{\theta}^*\right) = \left(\sigma^2\right)^{-k/2} \exp\Bigg[- \left(\frac{1}{2\sigma^2}\left(\boldsymbol{y}_{1:k} - \hat{\boldsymbol{y}}_{1:k}\right)^T\left(\boldsymbol{y}_{1:k} - \hat{\boldsymbol{y}}_{1:k}\right) + \lambda_1 V_1 + \lambda_2 V_2\right)\Bigg] \tag{13}$$

$$p_{c,\ PF}\left(y_k|\boldsymbol{\theta}_k^i\right) = \left(\sigma_k^i\sqrt{2\pi}\right)^{-1} \exp\left[- \left(\frac{1}{2\sigma_k^{i\,2}}\left(y_k - x_k^i\left(\boldsymbol{\beta}_{k^i}\right)\right)^2 + \lambda_1 V_1 + \lambda_2 V_2\right)\right] \tag{14}$$

where $V_1 = \sum_{k=1}^{T_p} \max[0, -\hat{y}_{m,k}]$, $V_2 = \sum_{k=1}^{T_p} \max[0, -\hat{y}_{c,k}]$ are the maximum violation of the two constraints. In the equation, λ_1 and λ_2 are the penalty parameters corresponding to the two constraint violations. In terms of numerical aspects, the physical constraint acts as a regularization term to prevent constraint violation.

4. Metrics for prognosis performance

Long-term RUL prediction faces significant challenges due to various sources of uncertainty, with measurement noise being one of them. This type of uncertainty is inherently random [38,39] and affects the model parameter estimation that depends on the observed data. Different sets of data with the same level of noise can result in different estimations. For instance, Fig. 6 illustrates prediction by two sets of measurement

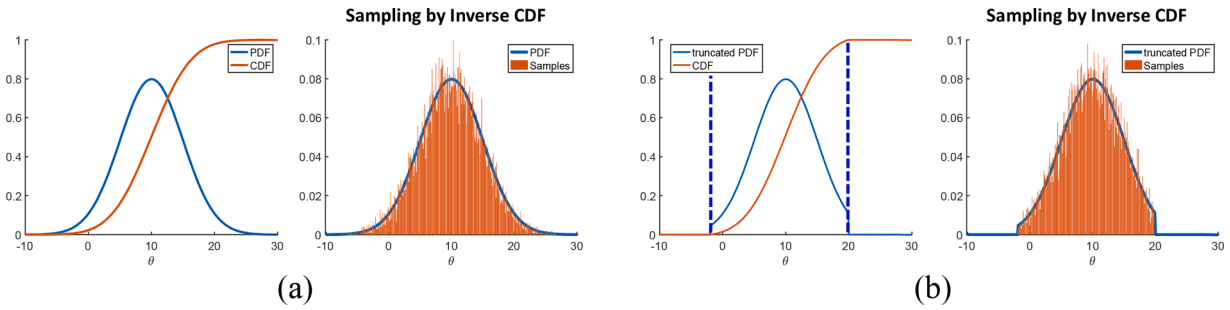

Fig. 5. Illustration of sampling by inverse CDF method from (a) general likelihood (b) truncated likelihood.

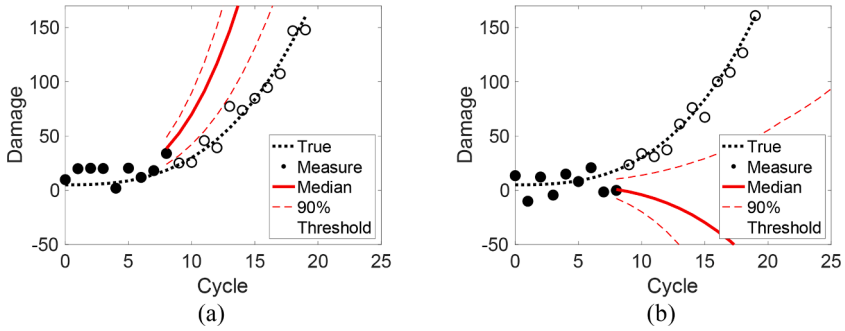

Fig. 6. Data uncertainty in measurement: (a) data under first random noise (b) second random noise.

generated from Eq. (7) with $\sigma \sim N(0, 10)$. The filled black circles represent the measured, and the red solid and dashed lines show the predicted median and 90 % C.I. using general BM, respectively. Despite the noise being added from the same distribution, the measured data appears different, leading to significantly different predictions. Therefore, the prediction performance using different datasets with the same level of noise need to be considered to evaluate data uncertainty in prediction.

4.1. Prediction accuracy quantification

The average RUL prediction accuracy is evaluated using the mean absolute error (MAE) defined as

$$MAE_k = \frac{1}{M}\sum_{i=1}^{M}\left|\widehat{RUL}_m(\boldsymbol{\theta}_k) - RUL_{True}(\boldsymbol{\theta}_k)\right| \tag{15}$$

where $\widehat{RUL}_m$ represents the median value of predicted RUL by estimated model parameters using measurements until cycle k, and RUL_{True} is true RUL value [29]. The MAE is computed by averaging over M datasets.

4.2. Prediction uncertainty quantification

From the perspective of decision-makers, in addition to the prediction accuracy. the uncertainty in RUL prediction offers a clearer understanding of the potential variability in the predicted RUL and help in making reliable maintenance decisions. In most of studies, uncertainty can be assessed by the C.I. of the predicted RUL [40]. However, owing to data randomness, the uncertainty bound itself can also have uncertainty. Therefore, it is vital for the prognostic algorithms to have consistent performance even under different test datasets. To quantify the consistency of the prognostic algorithm, the lower bound (5 percentile), median (50 percentile), and upper bound (95 percentile) of the RUL predictions of M datasets are stored as a table in Fig. 7. Then we additionally calculated the 90 % C.I. and median for M sets of predicted RULs and draw uncertainty of RUL curve with the shaded surface as in Fig. 7. The overall uncertainty is increased when data uncertainty is considered, and this uncertainty range should decrease to establish the appropriate decision-making. This approach was also studied in the previous study by the authors [19].

Besides the uncertainty visualization, quantification evaluation metrics are also used to measure the quality and convergence rate of the prediction. A predict interval coverage probability (PICP) is used to

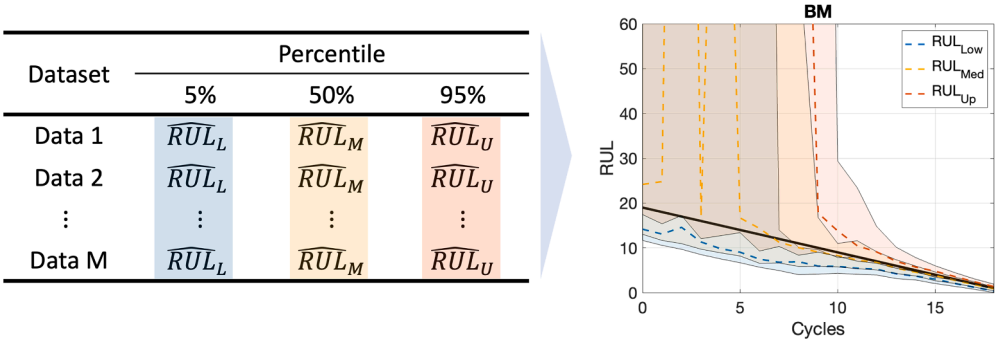

Fig. 7. Data uncertainty quantification in RUL curve.

evaluate the percentage of true RUL that falls within the given predicted C.I. [41,42].

$$PICP = \frac{1}{n}\sum_{i=1}^{n} c_i,\ c_i = \begin{cases} 1, & L_i \le RUL_i \le H_i \\ 0, & otherwise \end{cases} \tag{16}$$

L_i and H_i are the lower and upper bounds of prediction interval for every sample i, and c_i is used to judge whether the true RUL RUL_i is contained in the credible interval. In this study, the average PICP over M datasets are calculated which the larger the PICP is, the more actual RULs fall into the C.I., and the more reliable and the prediction results of the model are. The PICP should exceed the given confidence as much as possible.

The PICP alone can misunderstood the uncertainty information of RUL prediction accurately since too broad a PI can lead to high PICP value. Thus, it is necessary to consider the interval width to thoroughly evaluate the prediction uncertainty. Predict interval normalized average width (PINAW) calculates the average width of the C.I., which can be shown as

$$PINAW = \frac{1}{n(RUL_{\max} - RUL_{\min})}\sum_{i=1}^{n}(H_i - L_i) \tag{17}$$

where $RUL_{\max}$ and $RUL_{\min}$ denote the maximum and minimum of the true RUL respectively. The average PINAW value over M datasets is calculated. In case when PICP values are similar, the smaller PINAW, the better the prediction of the model [43].

5. Numerical case study

This section aims to demonstrate the proposed methods' effectiveness through a numerical study. Specifically, the nonlinear degradation data is generated using Eq. (7) where the true values of β_1 and β_2 are 0.05 and 0.02, respectively. The third-order polynomial function contains two stationary points that can represent the degradation process of the normal, initial degradation and sever degradation condition before failure. To account for moderate and severe noisy conditions, two values of σ (10 and 50) are considered, and 50 random datasets are generated to for each.

5.1. Prediction results

To apply physical constraint using Method 1, the initial prior distributions of the model parameters satisfying the constraints need to be identified. Fig. 8 illustrates this process. The initial range of the prior distribution is divided into 50×50 grid. In this example, the range is between -0.1 to 0.1 for both $\beta_j,\ j = 1,\ 2$. Then, $\widehat{y}_m$ and $\widehat{y}_c$ are calculated over the grid at each cycle. The prior distribution at a grid is defined as 1 if both $\widehat{y}_m$ and $\widehat{y}_c$ are positive, otherwise as 0. The results of grid at cycle 1 shows that β_1 should always be positive to satisfy the constraints. The prediction point T_p is set 50 cycles in this study and prior constraint range that meet the physical constraints over all cycles is found as $\mathbb{C} = \{0 \le \beta_j \le 0.1\}$ where $j = 1,\ 2$.

The degradation prediction using the conventional Bayesian prognosis algorithms and proposed methods are compared using data up to 8 cycles for estimation. Except for constraint Method 1, the initial prior distribution ranges for the parameters are set as below.

$$f(\beta_1) \sim U(-0.1,\ 0.1)\ \&\ f(\beta_2) \sim U(-0.1,\ 0.1)$$

Fig. 9(a) and (b) depict the results based on BM under small and large levels of noise, respectively. The general BM prediction is unsatisfactory because the estimated posterior state does not accurately reflect the true underlying degradation process due to noisy data. The median of the predicted distribution violates the monotonicity principle and yields a decreasing trend over cycles. In contrast, the predictions based on the proposed methods are satisfactory since the median of the predicted

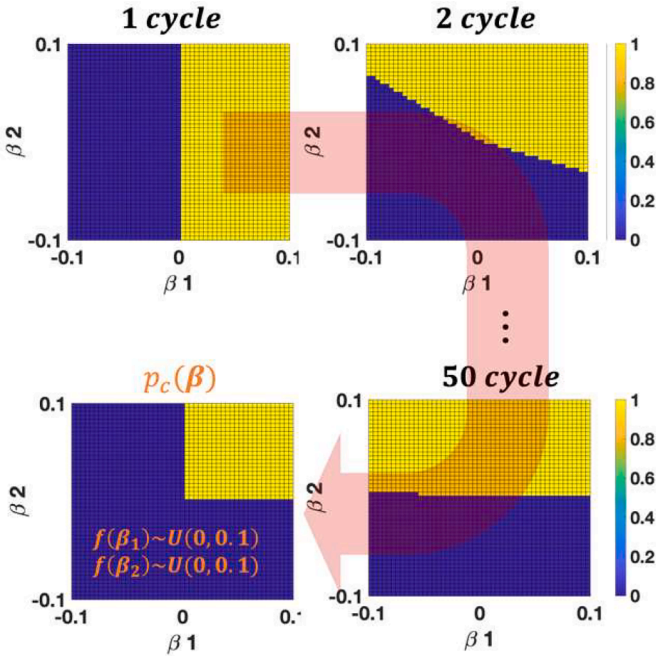

Fig. 8. The range of initial prior distributions that satisfy constraints at different cycles.

distribution is not only monotonically increasing but also close to the true degradation with reduced uncertainty. Fig. 10 shows the prediction results by RPF, and similar results are observed where constrained methods provide better performance. Thus, proposed constrained Bayesian framework with physical information avoids large prediction errors caused by local noisy data and predicts the degradation trajectory monotonically even under early prediction. Even if the median prediction from the large noise level seems more accurate than that of the small noise level, this is by accident due to the realization of noise.

5.2. Prediction performance analysis

In this section, we use the metrics introduced in Section 4 to compare the prediction accuracy. In Fig. 11(a), the MAE of 50 random datasets based on the BM is shown, where the column represents the MAE at each cycle and the row divided by different noise levels and methods. The results demonstrate that the proposed methods outperform the general BM, particularly in the early stages (5~9 cycles). However, under sufficient measurements until failure, the prediction accuracies of both general and constrained BM are not much different (15 cycles). The grey shaded column represents the overall MAE from 5 to 15 cycles, and our proposed method reduces the MAE significantly compared to the general BM. Moreover, under large noise data, the constrained methods show better performance even in the later stages. Fig. 11(b) shows the results of the RPF, addressing similar performance observed in the BM. The overall prediction accuracy of the general RPF is better than that of the general BM since more sampling errors can exist due to the random walk process in MCMC sampling [23].

Next, the RUL curve plots regarding the data uncertainty by BM and RPF are shown in Fig. 12. Fig. 12(a) illustrates the result of the BM under the small noise level. The black line indicates the true RUL value. The proposed constraint methods show a significant reduction in uncertainty and high accuracy in the earlier stages compared to the general BM. Under the large noise, the general BM is unable to provide robust predictions, while the proposed methods consistently predict the RUL with reduced uncertainty and the median close to the true one. The results by RPF are displayed in Fig. 13, with superior performance compared to the general RPF.

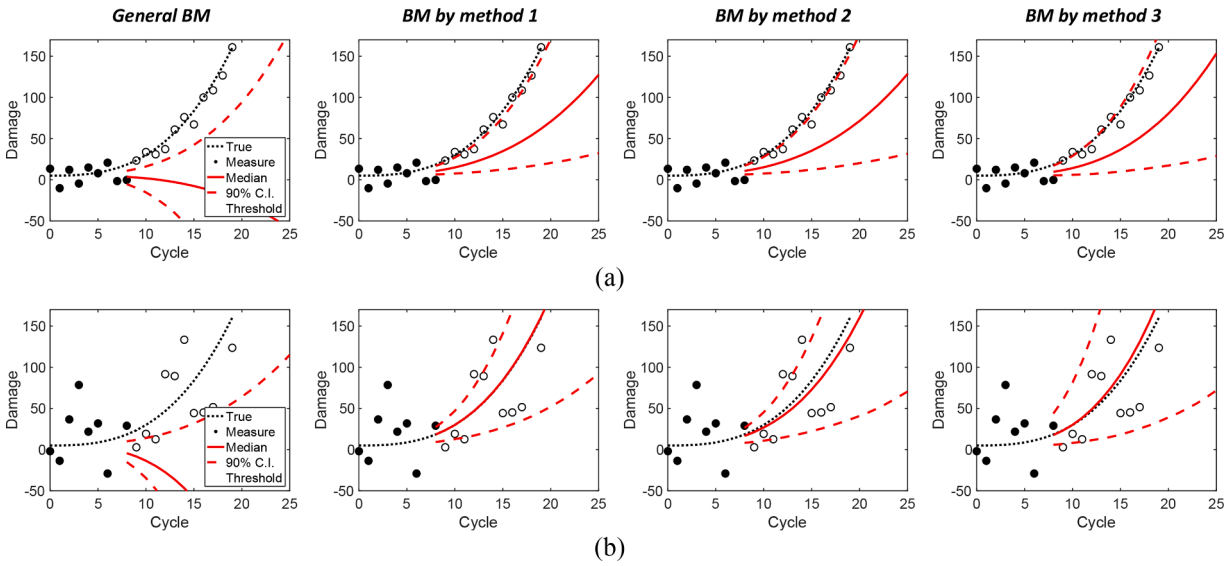

Fig. 9. Prediction results using BM and proposed constraint methods: (a) under small-level of noise (b) large-level of noise.

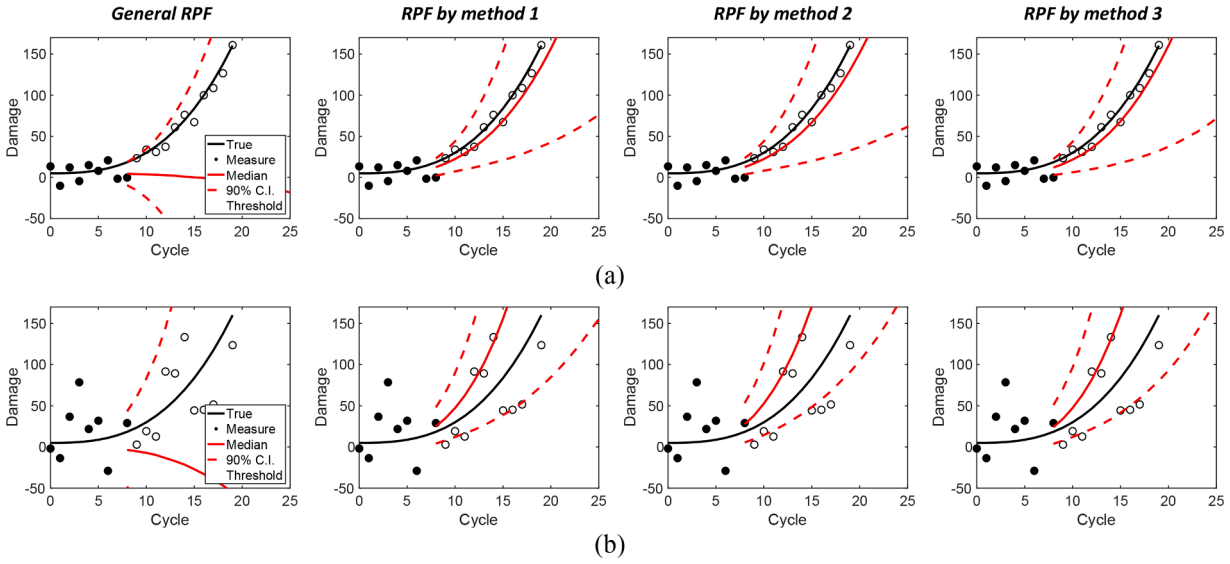

Fig. 10. Prediction results using RPF and proposed constraint methods: (a) under small-level of noise (b) large-level of noise.

	Method	MAE					
		5 cycle	⋯	*9 cycle*	⋯	*15 cycle*	*Overall (1 ~ 20)*
$\sigma = 10$	BM	172.89	⋯	21.35	⋯	0.61	452.38
	BM by method 1	3.57	⋯	2.85	⋯	0.63	28.67
	BM by method 2	3.84	⋯	2.56	⋯	0.63	28.79
	BM by method 3	3.92	⋯	2.60	⋯	0.65	28.81
$\sigma = 50$	BM	155.15	⋯	102.02	⋯	9.35	986.32
	BM by method 1	3.98	⋯	3.97	⋯	2.39	42.66
	BM by method 2	4.03	⋯	3.73	⋯	2.41	42.32
	BM by method 3	4.21	⋯	4.05	⋯	2.12	42.94

(a)

	Method	MAE					
		5 cycle	⋯	*9 cycle*	⋯	*15 cycle*	*Overall (1 ~ 20)*
$\sigma = 10$	RPF	108.06	⋯	21.97	⋯	0.71	271.60
	RPF by method 1	4.67	⋯	2.46	⋯	0.64	31.74
	RPF by method 2	4.50	⋯	2.65	⋯	0.64	32.28
	RPF by method 3	4.54	⋯	2.51	⋯	0.65	32.99
$\sigma = 50$	RPF	124.26	⋯	71.87	⋯	3.28	643.17
	RPF by method 1	4.62	⋯	4.54	⋯	2.10	44.72
	RPF by method 2	4.92	⋯	4.50	⋯	2.19	46.85
	RPF by method 3	4.74	⋯	4.48	⋯	2.12	46.30

(b)

Fig. 11. MAE of 50 random datasets by (a) BM and (b) RPF under different noise levels.

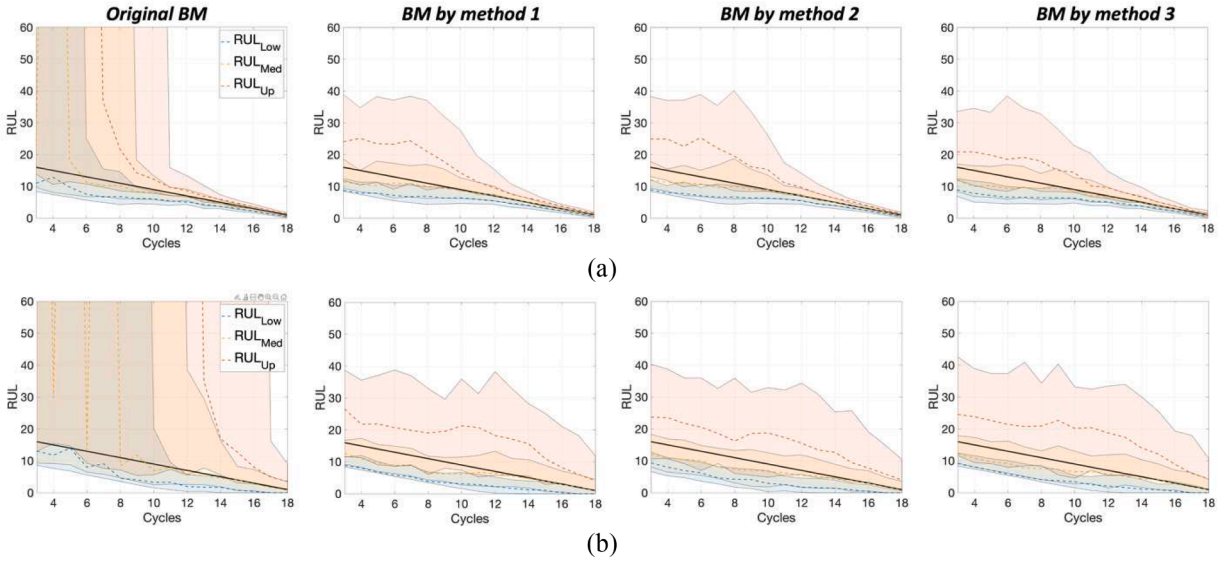

Fig. 12. RUL curve plot of 50 random datasets by (a) BM under small noise (b) BM under large noise.

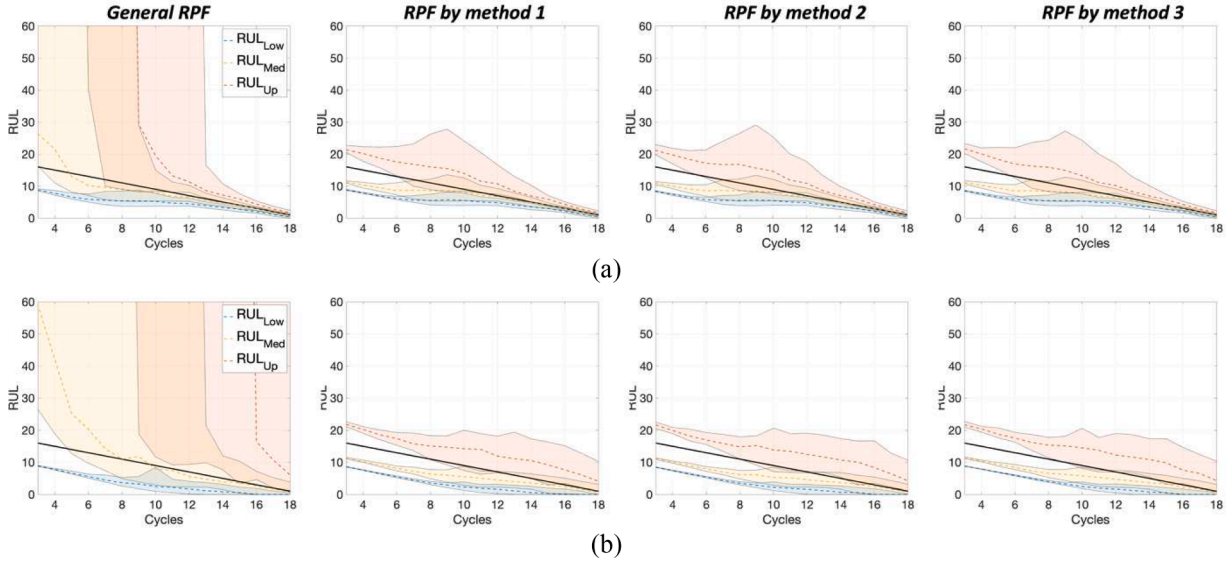

Fig. 13. RUL curve plot of 50 random datasets by (a) RPF under small noise (b) RPF under large noise.

It is noted that the uncertainty intervals for the constrained BM and RPF methods do not consistently decrease as more measurements are added but tend to become larger and then reduce after the steep section of the degradation curve. This behavior can be attributed to the presence of strong nonlinearity in the later stages, which has also been observed in the previous study [44].

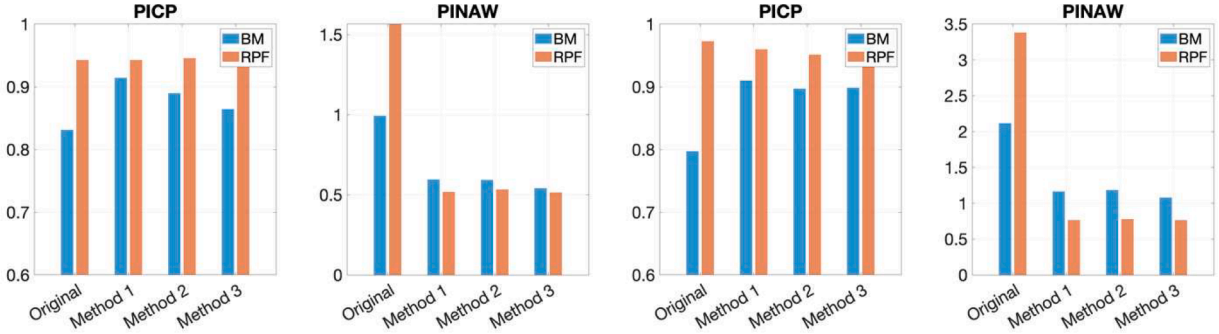

Fig. 14. Prediction interval results with different level of noise.

To further assess the prediction uncertainty performance, the average value of both PICP and PINAW are calculated from the 50 random datasets. The Fig. 14(a) illustrates the PICP and PINAW results for datasets with small level noise, with the blue and red bars representing BM and RPF, respectively. In PICP, the constrained BM method showed a significant increase indicating higher prediction interval coverage compared to general BM. The RPF consistently achieved high scores irrespective of the applied constraints. Regarding the width of the RUL prediction intervals, both BM and RPF with proposed methods, exhibited a substantial decrease in PINAW, with PINAW being at least 50 % smaller. These results emphasize that the proposed approaches can reduce the uncertainty of RUL predictions while maintaining stable prediction coverage.

The prediction results yield the following observations for each method. Firstly, Method 1, employing prior range constraints, is straightforward and suitable for low-dimensional degradation models. However, obtaining the prior distribution in high dimensions can be computationally challenging, and identifying feasible ranges satisfying constraints may be difficult. Secondly, Method 2, requiring no prior knowledge, has the potential to discard samples regardless of likelihood with measurements. Thirdly, Method 3 provides a regularization effect without losing any samples, but appropriate selection of penalty parameters is crucial. Despite these considerations, all proposed methods exhibit improved prediction performance compared to the conventional Bayesian framework, even under severe noise conditions. Method 1 is notable for determining the prior range through a combination of the damage model's monotonicity and curvature, unlike from traditional reliance on expert domain knowledge or experience. Both Method 2 and Method 3 offer the distinct advantage of directly truncating the posterior PDF during resampling, eliminating the need for subsequent truncation step and sample reduction in deriving the posterior distribution. In the following case study, BM and RPF using Method 3 is implemented owing to its high performance with the advantage of regularization effect, all while preventing the computational cost of identifying prior range and the risk of sample loss.

6. Case study

As a case study of the RUL prediction, a commercial quadcopter, a Parrot Mambo drone (PMD) is used which safety issues are increasing for fall-off by driving motors degradation. The PMD is a miniature quadcopter manufactured and sold by Parrot, France, measuring 7.1×7.1 inches with a mass of 63 g. The PMD is equipped with an 8520 coreless direct current (DC) motor and has a high-risk failure owing to the performance degradation of motors [45].

6.1. Experimental setup

For an accelerated life test, the takeoff and hovering motion at the altitude of 1.1 m with the rotational angles being 0 rad is performed with intermittent intervals. The PMD flight data are collected during the hovering test and the snapshot of takeoff and hovering motion with nominal motors are shown in Fig. 15(a). After 106 h of experiment, the degradation is incurred to motor 4 in the PMD which corresponds to 48 cycles of hovering tests with intervals. In contrast to the normal hovering motion which rises smoothly in the vertical direction, the hovering motion in Fig. 15(b) shows the difficulty to reach the target altitude as it greatly deviates from the vertical path. Degraded motor 4 in Fig. 15(d) shows foreign substances at the bottom of the brush and coil owing to the cumulated wear compared to a nominal motor in Fig. 15(c).

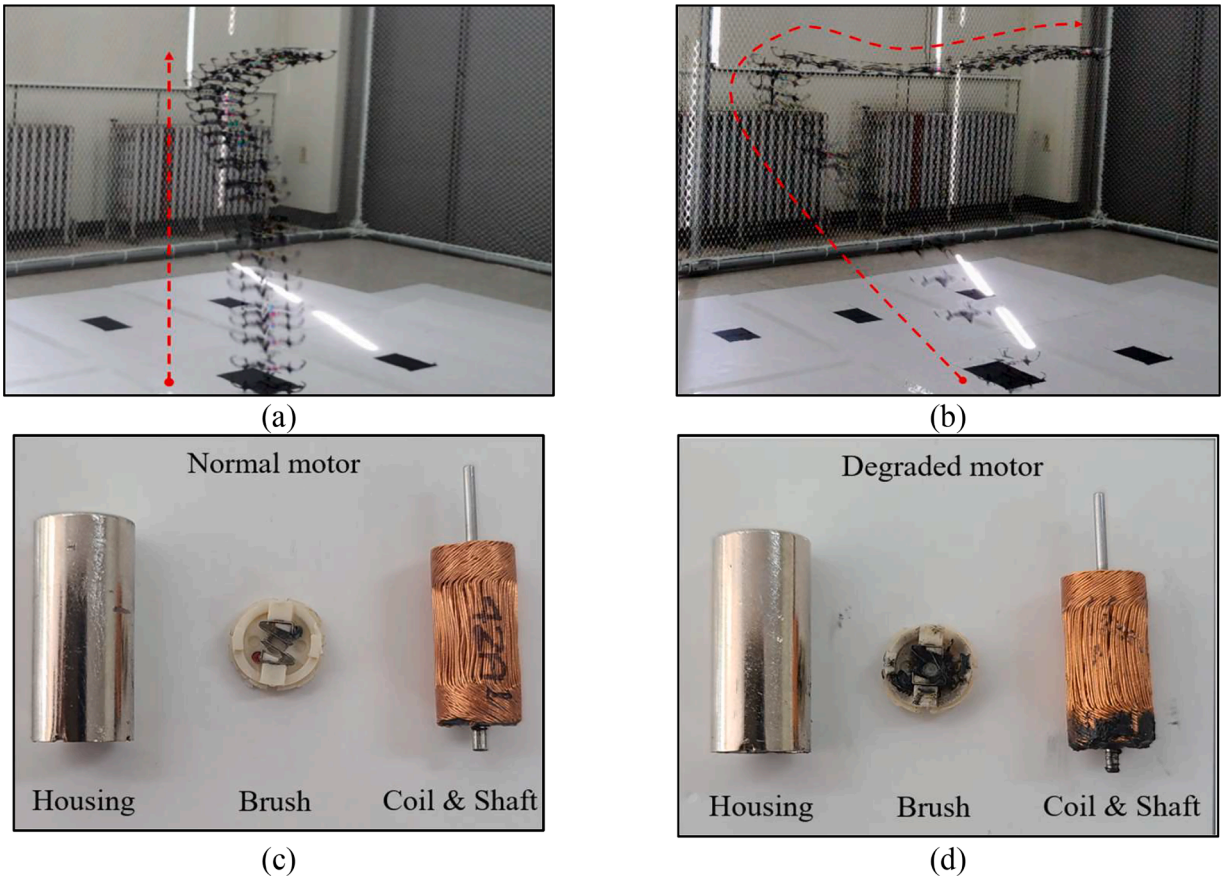

Fig. 15. (a) PMD take-off and hovering with normal motor (b) PMD take-off and hovering with degraded motor (c) components of normal motor (d) components of degraded motor.

The maximum thrust is selected as a health indicator (HI) for the motor, which is obtained by online estimation based on the Kalman filter (KF) at each cycle. The detailed process of HI estimation can be found in the previous research [46] and is considered beyond the scope of the current research goal. In Fig. 16, the blue circles and red-filled circles are the maximum thrusts of motor 1 (normal) and motor 4 (degraded) until 48 cycles. Motor 1 maintains its thrusts between 0.2434 to 0.2370, while motor 4 non-linearly decreases and reaches the threshold (magenta--colored line). Using these measurements, the RUL is predicted with BM and RPF by Method 3.

6.2. RUL prediction based on the proposed method

The empirical degradation model for motor is defined by the dual exponential function of cycles, as it is widely employed for the non-linearly degrading trend such as batteries [47–49]:

$$x_k = \beta_{1,k}\exp(\beta_{2,k}t_k) + \beta_{3,k}\exp(\beta_{4,k}t_k) \tag{18}$$

where x_k is the HI of the motor, t_k is the cycle index, and $\beta_{i,k}(i = 1, \ldots, 4)$ are the model parameters. Unlike the BM, the RPF requires the state and measurement model in a recursive form:

State transition model:

$$\boldsymbol{\theta}_k = \begin{bmatrix} x_{k-1}\cdot e^{\beta_{2,k}dt} + \beta_{3,k}e^{\beta_{4,k}t_k}\left(1 - e^{(\beta_{2,k}-\beta_{4,k})dt}\right) \\ \boldsymbol{\beta}_k \\ \sigma_k \end{bmatrix} + \boldsymbol{w}_k \tag{19}$$

Measurement model:

$$y_k = x_k + \epsilon \text{ with } \epsilon \sim N(0, \sigma) \tag{20}$$

where $dt = t_k - t_{k-1}$, $\boldsymbol{\theta}_k$ is the state variable including the thrust, the model parameters, and the measurement noise, namely, $\boldsymbol{\theta}_k = [x_k, \boldsymbol{\beta}_k, \sigma_k]^T$, and y_k is the measurement variable which is the estimated maximum thrust from the online estimation.

The initial prior distributions of the parameters for the BM and RPF procedures are assumed as follows, which is a rough range based on the degradation fitting over the entire cycles:

$$x_0 \sim U(0.23,\ 0.25),\ \beta_2 \sim U(0.05,\ 0.15),\ \beta_3 \sim U(0.2,\ 0.4)\ \beta_{1,\ 4} \sim U(-0.05,\ 0.05),\ \sigma \sim U(0, 0.1)$$

From these, 5000 samples/particles are generated to be used for the sampling in both BM and RPF. Moreover, considering the HI of motor to naturally decrease as degradation occurs, it requires to incorporate negative trend inequality constraints. It is worth highlighting that in various applications, each with its distnct domain knowledge and degradation characteristics, relevant constraints should be tailored.

$$\mathbb{C} = \{\widehat{y}_m \le 0\ \&\widehat{y}_c \le 0\}$$

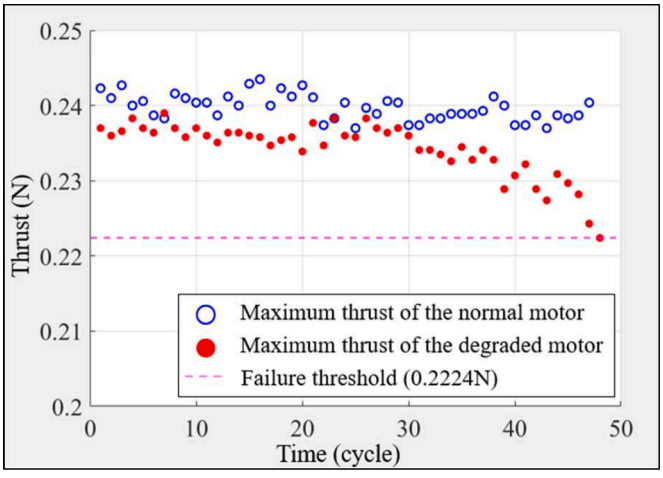

Fig. 16. Maximum thrust of motors at each cycle.

Fig. 17(a) and (b), respectively, show the prediction comparison conducted by BM and RPF using measurement until 24 cycles. In Fig. 17 (a), the red and blue dashed lines represent the medians of prediction by general and constrained BM, respectively. The dotted lines show the prediction interval (P.I.) with the estimated standard deviation. It is noticeable that the prediction by the general BM is affected by the local noisy data around 20–27 cycles giving a counter-intuitive prediction trajectory. Meanwhile, the proposed method shows improved prediction with narrower uncertainty bounds. Similar performance is also observed in RPF.

Furthermore, an RUL curve comparison was conducted between the prediction under a single exponential model, a dual exponential model, and a dual exponential model with constraint method. In Fig. 17(c), the yellow shaded area represents the predicted RUL with interval under the single exponential model. The two parallel black dotted lines indicate an allowable error bound (α%) around the true RUL, which is set at 10 % in this study. The results show that the single exponential model cannot accurately predict the RUL even using all measurements. The red shaded area represents the predicted RUL under the dual exponential model with the general BM, which predicts within the allowable error bound after 34 cycles while suffering from large fluctuations in the earlier stage predictions. On the other hand, the blue shaded area by the proposed constrained BM method shows reliable and accurate RUL prediction from 23 cycles, which is 11 cycles faster than the general BM. The RUL prediction curve by the RPF algorithm is also illustrated in Fig. 17(d) and shows superior performance similar to BM.

7. Conclusions

This study introduced three distinct approaches aimed at enhancing Bayesian inference-based prognostic algorithms by integrating constraints derived from low-fidelity physical information. These proposed methods effectively mitigate the adverse effects of local noisy data, resulting in significantly improved accuracy in predicting RUL, particularly in early-stage predictions. Furthermore, the approach takes into account data uncertainty, offering a comprehensive assessment of the accuracy and uncertainty quantification of predicted RUL values.

The effectiveness of our proposed approach is exemplified through both numerical examples and a real-world case study, where quantification metrics demonstrated the superior performance of our methods compared to the conventional Bayesian framework prognostic algorithms. Importantly, this framework underscores the adaptability and variability of our approach across various scenarios, emphasizing the importance of incorporating domain-specific knowledge when formulating constraints.

Future research efforts will prioritize on the automatic determination of optimal penalty parameters to enhance real-time performance. Additionally, extending the application of the proposed method to consider more than one degradation signals with constraints will provide broader utility as various signals are monitored simultaneously.

CRediT authorship contribution statement

Hyung Jun Park: Writing – original draft, Visualization, Validation, Methodology, Formal analysis, Conceptualization. **Nam H. Kim:** . **Joo-Ho Choi:** Writing – review & editing, Supervision, Conceptualization.

Declaration of competing interest

The authors declare that they have no known competing financial interests or personal relationships that could have appeared to influence the work reported in this paper.

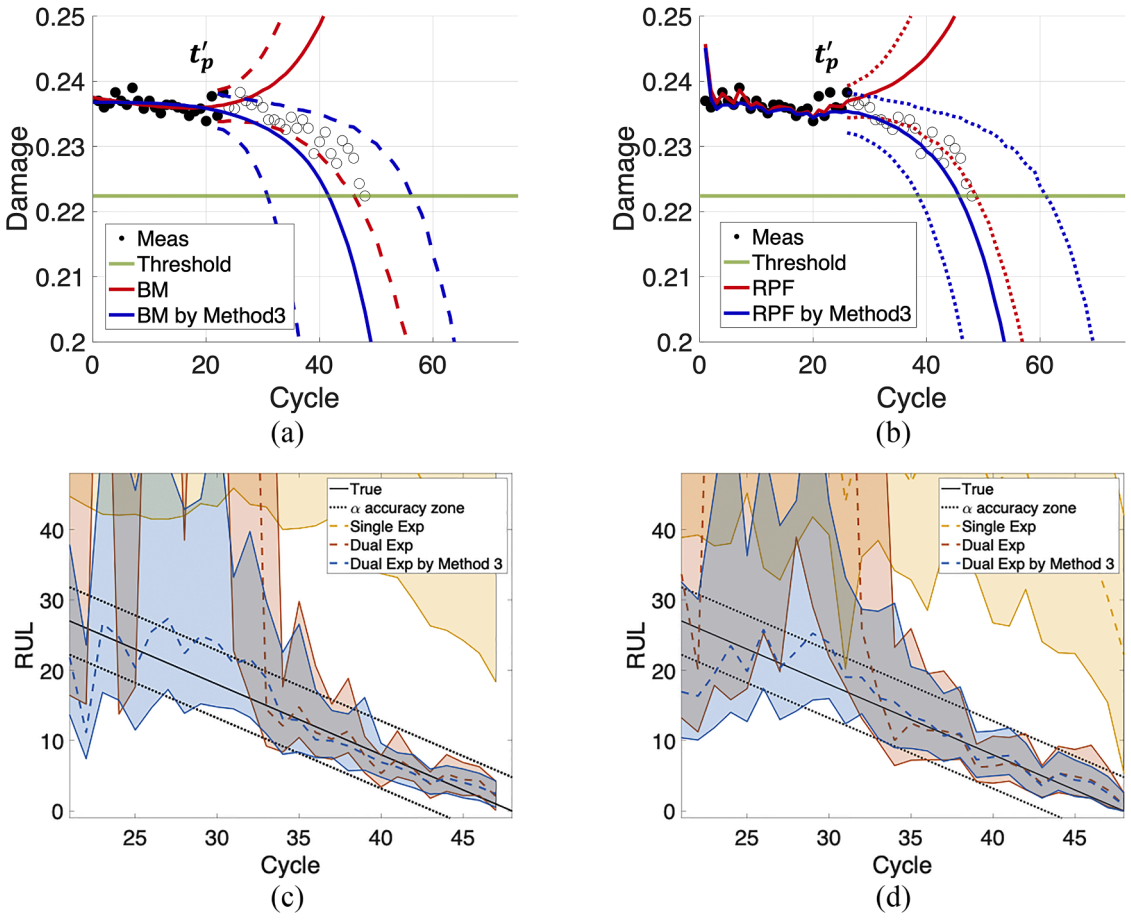

Fig. 17. Plot of prediction at 23 cycles (a) and (b); RUL curve comparison (c) and (d).

Data availability

The authors do not have permission to share data.

Acknowledgments

This research was supported by Korea Electric Power Corporation (Grant number:R22XO02-01) and the MOTIE (Ministry of Trade, Industry, and Energy) in Korea, under the Fostering Global Talents for Innovative Growth Program (P0017307) supervised by the Korea Institute for Advancement of Technology (KIAT).

Reference

[1] Shin I, et al. A framework for prognostics and health management applications toward smart manufacturing systems. Int J Precis Eng Manuf Green Technol 2018;5 (4):535–54. https://doi.org/10.1007/s40684-018-0055-0. Korean Society for Precision Engineering.

[2] Kim S, Kim NH, Choi JH. A study toward appropriate architecture of system-level prognostics: physics-based and data-driven approaches. IEEE Access 2021;9: 157960–72. https://doi.org/10.1109/ACCESS.2021.3129516.

[3] Sutharssan T, Stoyanov S, Bailey C, Yin C. Prognostic and health management for engineering systems: a review of the data-driven approach and algorithms. J Eng 2015;2015(7):215–22. https://doi.org/10.1049/joe.2014.0303.

[4] Cheng Y, Wu J, Zhu H, Or SW, Shao X. Remaining useful life prognosis based on ensemble long short-term memory neural network. IEEE Trans Instrum Meas 2021; 70. https://doi.org/10.1109/TIM.2020.3031113.

[5] Silva RE, et al. Proton exchange membrane fuel cell degradation prediction based on adaptive neuro-fuzzy inference systems. Int J Hydrogen Energy 2014;39(21): 11128–44. https://doi.org/10.1016/j.ijhydene.2014.05.005.

[6] Hou WJ, Peng Y. Adaptive ensemble gaussian process regression-driven degradation prognosis with applications to bearing degradation. Reliab Eng Syst Saf 2023;239. https://doi.org/10.1016/j.ress.2023.109479.

[7] Meng H, Geng M, Han T. Long short-term memory network with Bayesian optimization for health prognostics of lithium-ion batteries based on partial incremental capacity analysis. Reliab Eng Syst Saf 2023;236. https://doi.org/10.1016/j.ress.2023.109288.

[8] Manjurul Islam MM, Prosvirin AE, Kim JM. Data-driven prognostic scheme for rolling-element bearings using a new health index and variants of least-square support vector machines. Mech Syst Signal Process 2021;160. https://doi.org/10.1016/j.ymssp.2021.107853.

[9] Lei Y, Li N, Gontarz S, Lin J, Radkowski S, Dybala J. A model-based method for remaining useful life prediction of machinery. IEEE Trans Reliab 2016;65(3): 1314–26. https://doi.org/10.1109/TR.2016.2570568.

[10] Leem SH, An D, Choi JH. Bayesian parameter estimation for prognosis of crack growth under variable amplitude loading. Trans Korean Soc Mech Eng A 2011;35 (10):1299–306. https://doi.org/10.3795/KSME-A.2011.35.10.1299.

[11] An D, Choi JH, Kim NH. Identification of correlated damage parameters under noise and bias using Bayesian inference. Struct Health Monit 2012;11(3):293–303. https://doi.org/10.1177/1475921711424520.

[12] Liu S, Fan L. An adaptive prediction approach for rolling bearing remaining useful life based on multistage model with three-source variability. Reliab Eng Syst Saf 2022;218. https://doi.org/10.1016/j.ress.2021.108182.

[13] Kim S, Park HJ, Choi JH, Kwon D. A novel prognostics approach using shifting kernel particle filter of Li-Ion batteries under state changes. IEEE Trans Ind Electron 2021;68(4):3485–93. https://doi.org/10.1109/TIE.2020.2978688.

[14] Hu Y, Miao X, Si Y, Pan E, Zio E. Prognostics and health management: a review from the perspectives of design, development and decision. Reliab Eng Syst Saf 2022;217. https://doi.org/10.1016/j.ress.2021.108063.

[15] Zio E. Prognostics and health management (PHM): where are we and where do we (need to) go in theory and practice. Reliab Eng Syst Saf 2022;218. https://doi.org/10.1016/j.ress.2021.108119.

[16] Yucesan YA, Viana FAC. Hybrid physics-informed neural networks for main bearing fatigue prognosis with visual grease inspection. Comput Ind 2021;125. https://doi.org/10.1016/j.compind.2020.103386.

[17] Tang T, Yuan H. A hybrid approach based on decomposition algorithm and neural network for remaining useful life prediction of lithium-ion battery. Reliab Eng Syst Saf 2022;217. https://doi.org/10.1016/j.ress.2021.108082.

[18] Huang X, Peng Z, Tang D, Chen J, Zio E, Zheng Z. A physics-informed autoencoder for system health state assessment based on energy-oriented system performance. Reliab Eng Syst Saf 2024;242. https://doi.org/10.1016/j.ress.2023.109790.

[19] Kim S, Choi JH, Kim NH. Data-driven prognostics with low-fidelity physical information for digital twin: physics-informed neural network. Struct Multidiscip Optim 2022;65(9). https://doi.org/10.1007/s00158-022-03348-0.
[20] Xu Y, Kohtz S, Boakye J, Gardoni P, Wang P. Physics-informed machine learning for reliability and systems safety applications: state of the art and challenges. Reliab Eng Syst Saf 2023;230. https://doi.org/10.1016/j.ress.2022.108900.
[21] Kim S, Park HJ, Seo YH, Choi JH. A robust health indicator for rotating machinery under time-varying operating conditions. IEEE Access 2022;10:4993–5001. https://doi.org/10.1109/ACCESS.2022.3140755.
[22] Wang Q, Xu K, Kong X, Huai T. A linear mapping method for predicting accurately the RUL of rolling bearing. Measurement (Lond) 2021;176. https://doi.org/10.1016/j.measurement.2021.109127.
[23] Kim N-H, An D, Choi JH. Prognostics and health management of engineering systems. Switzerland: Springer International Publishing; 2017.
[24] Chen Y, He Y, Li Z, Chen L, Zhang C. Remaining useful life prediction and state of health diagnosis of lithium-ion battery based on second-order central difference particle filter. IEEE Access 2020;8:37305–13. https://doi.org/10.1109/ACCESS.2020.2974401.
[25] S. Liu and L. Fan, "An adaptive prediction approach for rolling bearing remaining useful life based on multistage model with three-source variability," *Reliab Eng Syst Saf*, vol. 218, 2022, 10.1016/j.ress.2021.108182.
[26] Meng F, Yang F, Yang J, Xie M. A power model considering initial battery state for remaining useful life prediction of lithium-ion batteries. Reliab Eng Syst Saf 2023;237. https://doi.org/10.1016/j.ress.2023.109361.
[27] Najera-Flores DA, Hu Z, Chadha M, Todd MD. A physics-constrained Bayesian neural network for battery remaining useful life prediction. Appl Math Model 2023;122:42–59. https://doi.org/10.1016/j.apm.2023.05.038.
[28] Sun X, Zhong K, Han M. A hybrid prognostic strategy with unscented particle filter and optimized multiple kernel relevance vector machine for lithium-ion battery. Measurement (Lond) 2021;170. https://doi.org/10.1016/j.measurement.2020.108679.
[29] Son J, Zhou S, Sankavaram C, Du X, Zhang Y. Remaining useful life prediction based on noisy condition monitoring signals using constrained Kalman filter. Reliab Eng Syst Saf 2016;152:38–50. https://doi.org/10.1016/j.ress.2016.02.006.
[30] Tang X, Liu K, Wang X, Liu B, Gao F, Widanage WD. Real-time aging trajectory prediction using a base model-oriented gradient-correction particle filter for Lithium-ion batteries. J Power Sources 2019;440. https://doi.org/10.1016/j.jpowsour.2019.227118.
[31] Downey A, Lui YH, Hu C, Laflamme S, Hu S. Physics-based prognostics of lithium-ion battery using non-linear least squares with dynamic bounds. Reliab Eng Syst Saf 2019;182:1–12. https://doi.org/10.1016/j.ress.2018.09.018.
[32] Yu H, Li H. Pump remaining useful life prediction based on multi-source fusion and monotonicity-constrained particle filtering. Mech Syst Signal Process 2022;170. https://doi.org/10.1016/j.ymssp.2022.108851.
[33] Li X, Teng W, Peng D, Ma T, Wu X, Liu Y. Feature fusion model based health indicator construction and self-constraint state-space estimator for remaining useful life prediction of bearings in wind turbines. Reliab Eng Syst Saf 2023;233. https://doi.org/10.1016/j.ress.2023.109124.
[34] Dong T, An D, Kim NH. Prognostics 102: Efficient Bayesian-based prognostics algorithm in MATLAB. Fault Detect. Diagn. and Prognosis 2019;20:5–25.
[35] Andrieu C, De Freitas N, Doucet A, Jordan MI. An introduction to MCMC for machine learning. Mach Learn 2003;50:5–43.
[36] D. An, J. Gang, and J.H. Choi, "MCMC approach for parameter estimation in the structural analysis and prognosis," 2010.
[37] Orchard ME, Vachtsevanos GJ. A particle-filtering approach for on-line fault diagnosis and failure prognosis. Trans Inst Meas Control 2009;31(3–4):221–46. https://doi.org/10.1177/0142331208092026.
[38] Sankararaman S. Significance, interpretation, and quantification of uncertainty in prognostics and remaining useful life prediction. Mech Syst Signal Process 2015;52–53(1):228–47. https://doi.org/10.1016/j.ymssp.2014.05.029.
[39] Wang P, Youn BD, Hu C. A generic probabilistic framework for structural health prognostics and uncertainty management. Mech Syst Signal Process 2012;28:622–37. https://doi.org/10.1016/j.ymssp.2011.10.019.
[40] Gebraeel N, Lei Y, Li N, Si X, Zio E, JDMD Editorial Office. Prognostics and remaining useful life prediction of machinery: advances, opportunities and challenges. J Dyn Monit Diagn Feb. 2023. https://doi.org/10.37965/jdmd.2023.148.
[41] Rigamonti M, Baraldi P, Zio E, Roychoudhury I, Goebel K, Poll S. Ensemble of optimized echo state networks for remaining useful life prediction. Neurocomputing 2018;281:121–38. https://doi.org/10.1016/j.neucom.2017.11.062.
[42] Li X, Mba D, Lin T, Yang Y, Loukopoulos P. Just-in-time learning based probabilistic gradient boosting tree for valve failure prognostics. Mech Syst Signal Process 2021;150. https://doi.org/10.1016/j.ymssp.2020.107253.
[43] Yan X, Liang W, Xu D. Remaining useful life interval prediction for complex system based on BiGRU optimized by log-norm. IEEE Access 2022;10:108089–102. https://doi.org/10.1109/ACCESS.2022.3212694.
[44] Wang Y, Gogu C, Kim NH, Haftka RT, Binaud N, Bes C. Noise-dependent ranking of prognostics algorithms based on discrepancy without true damage information. Reliab Eng Syst Saf 2019;184:86–100. https://doi.org/10.1016/j.ress.2017.09.021.
[45] Susini A. A technocritical review of drones crash risk probabilistic consequences and its societal acceptance. RIMMA Risk Inf Manage Risk Models Appl. 2015;7:27–38.
[46] Lee D, Park HJ, Lee D, Lee S, Choi J-H. A novel Kalman Filter-based prognostics framework for performance degradation of quadcopter motors. IEEE Trans Instrum Meas 2023. https://doi.org/10.1109/TIM.2023.3332389. 1–1.
[47] Xing Y, Ma EWM, Tsui KL, Pecht M. An ensemble model for predicting the remaining useful performance of lithium-ion batteries. Microelectron Reliab 2013;53(6):811–20. https://doi.org/10.1016/j.microrel.2012.12.003.
[48] He W, Williard N, Osterman M, Pecht M. Prognostics of lithium-ion batteries based on Dempster-Shafer theory and the Bayesian Monte Carlo method. J Power Sources 2011;196(23):10314–21. https://doi.org/10.1016/j.jpowsour.2011.08.040.
[49] Lin J, Wei M. Remaining useful life prediction of lithium-ion battery based on auto-regression and particle filter. Int J Intell Comput Cybern 2020;14(2):218–37. https://doi.org/10.1108/IJICC-09-2020-0131.